Article

Photocatalytic Degradation of Crystal Violet (CV) Dye over Metal Oxide (MOx) Catalysts

Mohammed Sifat [1], Eugene Shin [1], Anthony Schevon [1], Hugo Ramos [1], Amol Pophali [1], Hye-Jung Jung [2], Gary Halada [1], Yizhi Meng [1], Nicholas Olynik [1], David J. Sprouster [1] and Taejin Kim [1,*]

[1] Department of Materials Science and Chemical Engineering, Stony Brook University, Stony Brook, NY 11794, USA; mohammed.sifat5301@gmail.com (M.S.); eugeneshin01@gmail.com (E.S.); anthony.schevon@gmail.com (A.S.); haramos2024@gmail.com (H.R.); amol.pophali@stonybrook.edu (A.P.); gary.halada@stonybrook.edu (G.H.); yizhi.meng@stonybrook.edu (Y.M.); nicholas.olynik@stonybrook.edu (N.O.); david.sprouster@stonybrook.edu (D.J.S.)

[2] Da Vinci College of General Education, Chung-Ang University, Seoul 06874, Republic of Korea; jayjung@cau.ac.kr

* Correspondence: taejin.kim@stonybrook.edu

Abstract: Crystal violet (CV) is an organic chloride salt and a triphenylmethane dye commonly used in the textile processing industry, also being used as a disinfectant and a biomedical stain. Although CV is widely used, it is carcinogenic to humans and is retained by industrial-produced effluent for an extended period. The different types of metal oxide (MOx) have impressive photocatalytic properties, allowing them to be utilized for pollutant degradation. The role of the photocatalyst is to facilitate oxidation and reduction processes by trapping light energy. In this study, we investigated different types of metal oxides, such as titanium dioxide (TiO_2), zinc oxide (ZnO), zirconium dioxide (ZrO_2), iron (III) oxide (Fe_2O_3), copper (II) oxide (CuO), copper (I) oxide (Cu_2O), and niobium pentoxide (Nb_2O_5) for the CV decomposition reaction at ambient conditions. For characterization, BET and Raman spectroscopy were applied, providing findings showing that the surface area of the anatase TiO_2 and ZnO were 5 m^2/g and 12.1 m^2/g, respectively. The activity tests over TiO_2 and ZnO catalysts revealed that up to ~98% of the dye could be decomposed under UV irradiation in <2 h. The decomposition of CV is directly influenced by various factors, such as the types of MOx, the band gap–water splitting relationship, and the recombination rate of electron holes.

Keywords: band gap; crystal violet; heterogenous catalyst; photocatalysis; recombination rate; water splitting

1. Introduction

Crystal violet (CV), also known as methyl violet 10B, hexamethyl pararosaniline chloride, or Gentian violet, is an aniline-derived dye that has been extensively used as a disinfectant, a biomedical stain, a pH indicator, and in the textile industry as a dye [1,2]. Despite CV's usefulness, the dye acts as a mitotic poison, a potent carcinogen, and a potent clastogen that promotes tumor growth in some species of fish, confirming its negative harmful impacts on the environment and human health [3]. For instance, CV exhibits an oral toxicity level (LD_{50}) of 1.2 g/kg for mice and 1.0 g/kg for rats [4]. For humans, CV can cause skin irritation, digestive tract irritation, and, in extreme cases, respiratory and kidney failure [3]. Considering the extensive applications of CV in daily life and its use for industrial purposes, CV cannot simply be substituted. Considering its toxic behavior, it is necessary for it to undergo degradation processes to convert it into less harmful compounds, such as CO_2 and H_2O, prior to disposal [5].

Different catalytic methods have been explored as a means of degrading dyes from industrial wastewater. In the recent past, ozonation of the dye compound has proved to be an effective strategy for achieving decomposition [6,7]. The molecular ozone can react with

produced hydroxyl radicals for the decomposition of chromophoric dyes into colorless entities. To improve the effects of the ozonation process, the use of activated carbon coupled with iron allows for enhanced catalytic activity due to activated carbon's high activity [8]. The ozonation reaction, however, holds several disadvantages, such as the toxicity of the ozone, as well as its high production cost and low utilization, thus increasing the need for more effective alternative methods. Biological methods of dye degradation, such as the use of cyanobacteria, have been explored, but they have yielded inconsistent and inefficient results in terms of their ability to degrade organic dyes [9].

Homogeneous and heterogeneous photocatalysis is widely popular due to its effectiveness, environmental friendliness, and ability to control the pollution of biological contaminants [10–12]. A homogeneous approach features a molecular or inorganic compound as the catalyst that is dissolved in the dye solution [13–15]. Since the catalyst is uniformly dispersed, the number of collisions between reactants and catalyst is at the maximum, which leads to fast reaction speeds and provides a good conversion rate per molecule of the catalyst. The major drawback in homogenous catalysis is the separation of the catalyst, which requires a strenuous and expensive process. This can be overcome via the heterogeneous catalysis approach, which involves using the catalyst and reactant in different phases (i.e., liquid–solid phase), and the reactant is adsorbed on the active surface of the catalyst. The advantages of heterogeneous catalysis include the reusability of catalysts with minimal loss and the low toxicity of catalysts [16,17]. Unlike other water treatment techniques, such as disinfection, filtration, and sedimentation, heterogeneous photocatalysis completely eliminates the contaminants rather than transforming them from one phase to another [18,19]. In the recent past, different types of metal oxide (MO_x) have emerged as cost-effective heterogeneous photocatalysts due to their reusability potential and wide applicability. Previous studies involving metal oxides have focused on doping and intercalating them with other materials, such as graphite, to improve their photocatalytic ability to decompose organic dyes [20,21]. The use of metal oxides on their own, however, to the authors' knowledge, has not been studied extensively for photocatalysis, especially with various types of MO_x, and it is believed that this approach is an effective heterogeneous catalysis method for the degradation of dye chemicals, including CV.

In the present work, the effect of different types of MO_x (TiO_2, ZnO, ZrO_2, Fe_2O_3, CuO, Cu_2O, and Nb_2O_5) as photocatalysts for CV degradation is studied. Heterogeneous catalysts such as TiO_2 and ZnO are known for their uses in several other applications in photocatalysis, as they are used for air and water purification, as disinfectants, as solar cells, and as photoluminescent devices [22,23]. It is worthwhile to note that the tested catalysts cover a broad range of band gaps (i.e., 1.7 eV to 5.0 eV) that are directly and indirectly related to the catalytic performance [24]. Screening of the broad range of catalysts was performed to evaluate the effect of changes in band gap energies required for the propagation of the redox reactions required to degrade organic dyes such as CV. Furthermore, the activity results have been related to important scientific factors such as band gap, water splitting, and recombination rate. Additionally, the catalysts were subjected to required physical property characterizations.

2. Results and Discussion

2.1. Catalytic Activity

A calibration plot with varying CV concentrations was obtained as a reference (Figure 1a). The line of best fit was utilized to find the equation that best correlates the absorbance to the concentration of the CV. As shown in Figure 1b,c, TiO_2 and ZnO successfully decomposed the CV, while other metal oxides, such as CuO, Cu_2O, ZrO, Nb_2O_5, and Fe_2O_3, showed no catalytic performance (Figure 1d). TiO_2 and ZnO showed 95% and 98% CV conversion, respectively, within 2 h (Figure 1e). C. Shaoo et al. studied photocatalytic activity for CV decomposition over bulk TiO_2 and Ag^+-doped TiO_2 to understand the effect of Ag^+ on catalytic performance [25]. Although the Ag^+-doped TiO_2 showed the advantage of easy separation compared to the TiO_2, the conversion of CV over two catalysts was similar:

for the TiO$_2$, it was ~97% within ~2 h, and for the Ag$^+$-doped TiO$_2$, it was ~99% within ~2 h. Recently, M.G. Sanakousar et al. investigated the decomposition of CV over ZnO and Cd-ZnO (mol% of Cd = 0.5~2.0%) catalysts and reported a high efficiency of bulk ZnO and Cd (0.5%)-ZnO (~92% CV conversion at 120 min), while ≥1.0% Cd reportedly leads to comparatively lower photocatalytic activity (80~85% CV conversion) [26]. The authors claimed that increasing electron hole recombination rates and multiple charge carriers' trapping phenomena cause a decrease in catalytic performance. For comparison purposes, dye chemicals' decomposition over ZnO and TiO$_2$ have also been reported [27,28]. D. R. Shinde et al. studied the photocatalytic degradation of CV, basic blue (BB), and methyl red (MR) under solar irradiation over ZnO, TiO$_2$, and SnO$_2$ and reported that ZnO showed the highest photocatalytic activity, followed by TiO$_2$ and SnO$_2$ [27]. The specific surface area of ZnO (~12 m^2/g) was higher than that of TiO$_2$ (~5 m^2/g), which, coupled with the greater quantum efficiency of ZnO compared to TiO$_2$, explains its higher overall photocatalytic performance. The difference between the results for the stock 10^{-5} M CV solution and for after the addition of the respective catalysts (TiO$_2$ or ZnO) and UV light irradiation source indicates that a larger number of moles were adsorbed following the prestir step of the experimental protocol for the TiO$_2$ sample compared to the ZnO sample (Figure 1b,c). The CV decomposition results depicted in Figure 1d are well matched to the reported ones, as highlighted in Table 1. Figure 1f shows the visual decolorization of CV during the reaction with the TiO$_2$ catalyst. The intensity of the CV color (purple) faded with increasing reaction time.
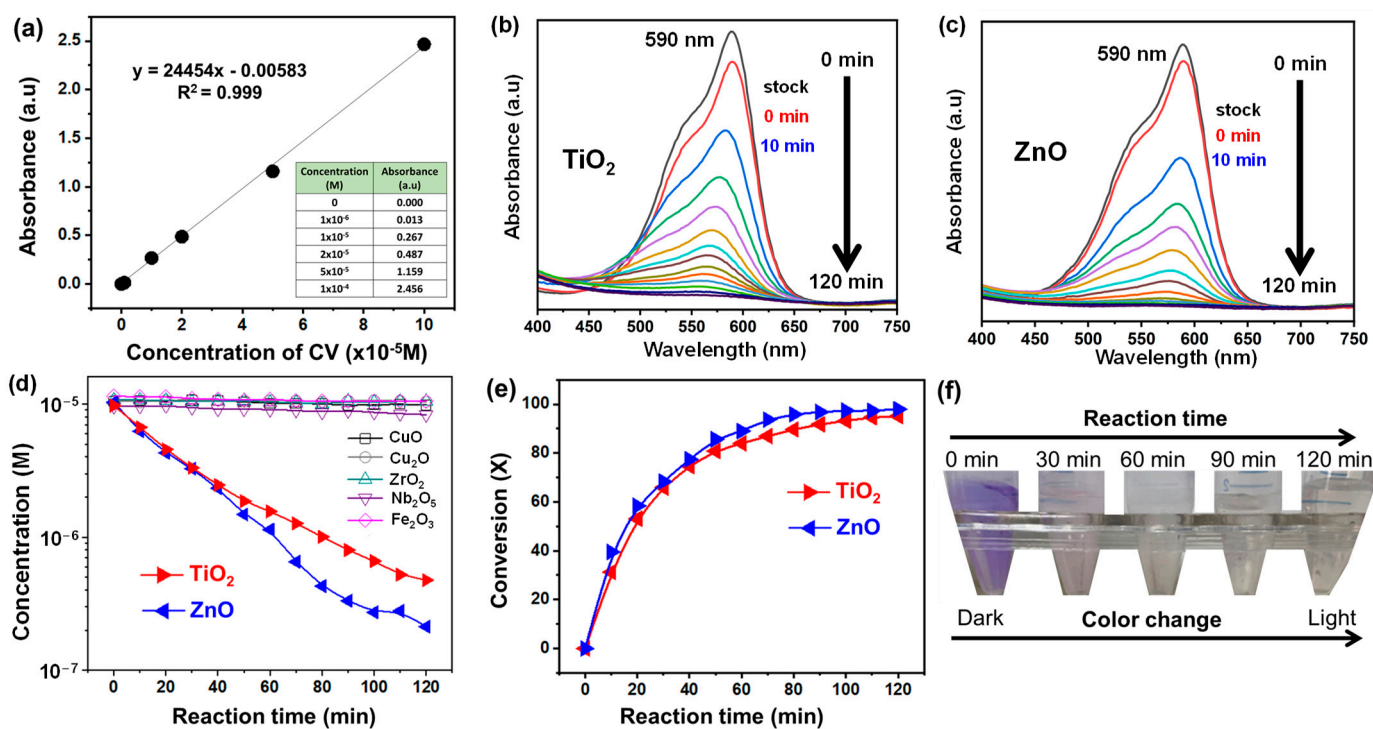
Figure 1. (**a**) Calibration curve with varied CV concentrations and absorbance spectra at 10 min intervals for selected metal oxides. (**b**) UV–visible spectra of CV solution from stock concentration (10^{-5} M) with no irradiation to after the addition of TiO$_2$ and UV light during the progression of the reaction over 120 min indicated by different colored spectra for each 10-min interval. (**c**) UV–visible spectra of CV solution from stock concentration (10^{-5} M) with no irradiation to after the addition of ZnO and UV light during the progression of the reaction over 120 min indicated by different colored spectra for each 10-min interval. (**d**) Change in concentration of CV dye solution over tested metal oxides. (**e**) Conversion of CV during the reaction's progression, and (**f**) visualization of CV decomposition over time. Reaction conditions: 25 mg of TiO$_2$ and 50 mL of 10^{-5} M CV solution under UV irradiation (365 nm).

Table 1. Catalytic performance comparison with previous works for the degradation of common organic dyes (i.e., CV, MB) under light irradiation.

| Catalyst	Energy Source	Band Gap (eV)	Dye	Initial Dye Concentration (ppm)	Irradiation Time (min)	Conversion (%)	Ref.
TiO_2	UV	3.2	CV	20	105	>97	[25]
Ag^+/TiO_2	UV	--	CV	20	105	>99	[25]
TiO_2	UV	3.2	CV	40	105	>88	[25]
Ag^+/TiO_2	UV	--	CV	60	105	>56	[25]
ZnO	UV	3.31	MB	40	40	67	[29]
GO/ZnO	UV	3.22	MB	40	40	89	[29]
ZnO	Visible	2.81	CV	5	240	82	[30]
ZnO/GO	Visible	2.71	CV	5	240	99	[30]
CuO	UV	1.29	MB	6120	120	50	[31]
CuO-ZnO	UV	1.23	MB	6120	120	94	[31]
TiO_2	UV	3.2	CV	4	120	95	Present study
ZnO	UV	3.2	CV	4	120	98	Present study

2.2. MO$_x$ Catalyst Choice Rationale for Dye Chemical Decomposition

2.2.1. Effect of Band Gap Energies on CV Decomposition

As shown in Figure 1d, the different MO_x (M = Zn, Ti, Cu, Zr, Nb, and Fe) catalysts show different CV decomposition catalytic performances. To understand the relationship between dye chemical decomposition and the types of MO_x catalysts, several parameters (i.e., specific surface area, band gap, and water splitting energy gap) should be considered. MO_x can be classified into three major types: semiconductors, conductors, and insulators. Semiconductors are increasingly useful materials for heterogeneous photocatalysis. Recent studies involving semiconductors are focused on narrowing the band gap, which is the energy difference between the valence band (VB) and the conduction band (CB) of the metal oxide, through changes in their physical structure [16,32]. Band gap is a vital parameter in determining the applicability of a semiconductor in a specific photocatalytic reaction because different photocatalytic reactions require specific band gap energies, including the reaction with CV [33]. Providing sufficient energy to the metal oxide allows for the formation of electron–hole (e_{CB}^-—electron in the CB, h_{VB}^+—hole in the VB) pairs, which effectively increase the rate of dye chemical decomposition. The overall reaction can be modeled as follows: $h_{VB}^+ + dye\ (CV) \rightarrow CV\ radical \rightarrow CV\ decomposition$. The required energy for overcoming the band gaps can be obtained from light, such as visible and UV light: $E\ (eV) = \frac{hc}{\lambda\ (nm)}$, where E is photon energy, h is Planck's constant, c is the speed of light, and λ is the wavelength of the supplied light.

Figure 2 shows the band gap energies of various metal oxides based on potentials. Since a 365 nm UV light, which is equivalent to 3.4 eV, was used in this research, it is hypothesized that a MO_x with >3.4 eV should show little or no catalytic activity due to its higher band gap energy compared to the applied energy. TiO_2 and ZnO both have a band gap energy of 3.2 eV, with the range also being covered in the water splitting energy gap range, allowing for degradation to occur under the supplied UV irradiation source. As such, it is also true that visible light (400–700 nm; 1.77–3.1 eV) does not provide sufficient energy for the working catalysts, as the minimum working band gap of the TiO_2 and ZnO catalysts is 3.2 eV. As shown in Figure 1d, Nb_2O_5 (3.5 eV) and ZrO_2 (5.0 eV) showed no CV decomposition, which is well matched to the band gap vs. dye chemical decomposition relationship. In the cases of Fe_2O_3 (2.1 eV), CuO (1.7 eV), and Cu_2O (2.2 eV), however, the relationship cannot explain the lack of CV decomposition over the catalysts, although

their band gap energies are much lower than 3.4 eV. To explain the results, the relationship between band gap and CV decomposition, along with another parameter known as the water splitting energy gap, should be considered.
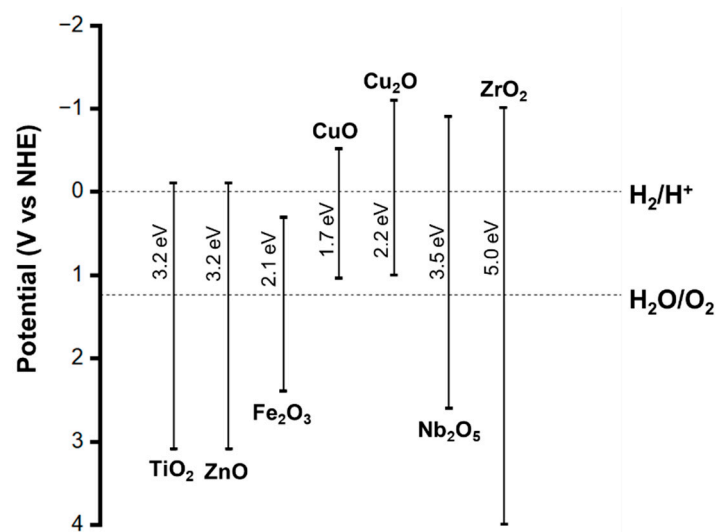
Figure 2. Pivotal properties of metal oxides for the decomposition reaction. Band gap energies of tested metal oxides vs. the normal hydrogen electrode (NHE), along with the known values for water splitting (E = 1.23 eV) [23].

2.2.2. Importance of Water Splitting Reaction

Among several key parameters, the potential energy of water splitting or hydroxyl (OH^-) or hydroxyl radical ($OH\bullet$) generation is an important aspect of dye degradation [34–36]. The water splitting reaction begins with the excitation of the electrons on the MO_x through photons emitted by UV irradiation. The resulting electron hole on the MO_x becomes an active site [37,38]. The ionization of the water occurs when water interacts with the electron hole in the VB and ionizes into a proton (H^+) and an $OH\bullet$ [38] The formation of the $OH\bullet$ is especially crucial for dye decomposition, as it is a strong oxidizing agent. Simultaneously, superoxide ($O_2^{\bullet-}$) is formed when oxygen gas interacts with the electron in the CB. This $O_2^{\bullet-}$ will then become protonated to form a hydroperoxyl radical ($HOO\bullet$) which will further dissolve into $OH\bullet$ [38]. Consequently, the chemical decomposition of the dye occurs by its interaction with $OH\bullet$, producing CO_2, H_2O, and other intermediates [34,38]. The dye can also interact with the electron hole in the VB and the electron in the CB to form oxidation and reduction products as well [38]. The water splitting energy gap (0–1.23 eV) range must be within the band edges of the selected MO_x, allowing the catalyst surface to interact with and facilitate the reaction.

The water splitting reaction is directly influenced by the recombination of electron–hole pairs that are generated due to the absorption of photons [39]. In recombination, electrons release the energy absorbed from photons and return from the CB to the VB, thus recombining and filling the electron hole generated during photocatalysis. Photocatalysts suffer from low efficiency due to serious charge-carrier recombination [39]. Thus, to drive efficient water splitting, charge separation in catalyst particles must proceed within the timescales of photoexcited carrier recombination [39]. As shown in Figure 2, Fe_2O_3, CuO, and Cu_2O are each outside of the water splitting range, resulting in their lack of photocatalytic activity [Figure 1d]. Based on the band gap and water splitting parameters of MO_x, it is indicated that only TiO_2 and ZnO could enable the decomposition of the CV dye with great efficiency.

2.3. Material Characterization

Raman spectroscopy has been applied to understand molecular structures, oxidation states, and the phases of metal oxide catalysts [40–43]. Figure 3a,b shows the Raman spectra

of TiO_2 and ZnO, the most effective catalysts for CV decomposition among the tested types of MO_x, with the peaks indicating the Raman-active modes of each catalyst, respectively. In Figure 3a, strong (s) and weak (w) intensity peaks at 144 (s), 200 (w), 398 (s), 518 (s), and 642 (s) cm^{-1} are assigned to the E_g, E_g, B_{1g}, A_{1g}/B_{1g} and E_g modes, respectively [44,45]. Based on the peak positions and relative peak intensity, it is confirmed that the tested TiO_2 contains the anatase phase [45–48]. In the case of ZnO, there are peaks at 102 (s), 333 (w), 439 (s), 586 (w), and 667 (w), which are assigned to the $E_2(LO)$, $E_2(LO)$-$E_2(H)$, $E_2(H)$, $E_1(LO)$, and $E_2(LO)$-$E_2(H)$ modes of Zincite, respectively [49–52]. The specific interactions present at each peak are summarized in Table 2. The Raman spectra of TiO_2 and ZnO are like previous studies' results [44,49,53,54].
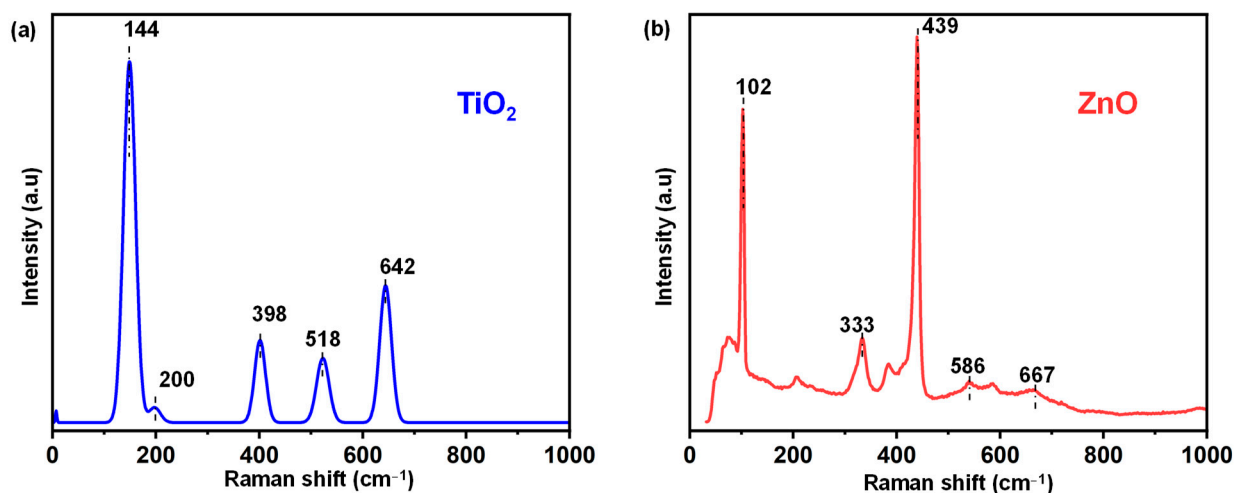
Figure 3. Raman spectra for (**a**) titanium dioxide (TiO_2) and (**b**) zinc oxide (ZnO).

Table 2. Raman shifts and the specific types of interaction.

Raman Shift (cm^{-1})	Raman Active Mode TiO_2	Raman Shift (cm^{-1})	Raman Active Mode ZnO
44	E_g—(symmetric stretching vibration)	102	E_{2L}—(nonpolar, low-intensity mode)
200	E_g—(symmetric stretching vibration)	333	$3E_{2L} - E_{2H}$
398	B_{1g}—(symmetric stretching mode)	439	E_{2H}—(nonpolar, high-intensity mode)
518	A_{1g}—(anti-symmetric bending vibration of O-Ti-O)	586	$E_1 (LO)$—(polar, longitudinal optical mode)
642	E_g—(symmetric stretching vibration)	667	$2(E_{2H} - E_{2L})$

XRD analysis of the working bulk catalysts (TiO_2 and ZnO) was conducted for the confirmation of the material, and SEM-EDX analysis was performed for the determination of the surface morphology of the material. Based on the identified miller indices in the experimental XRD patterns shown in Figure 4a,b, the presence of indices in the (101), (004), (200), (105), (211), and (204) planes indicated that the highly crystalline TiO_2 specimen was identified as anatase (Tetragonal, I41/amd) [55]. The ZnO sample, on the other hand, based on the identified miller indices at the (100), (002), (101), (102), (110), and (103) planes, was identified as Zincite (Hexagonal, P63mc) [56]. SEM-EDX analysis was used to determine the surface morphology of the samples, confirming that the particles sizes of the bulk material were <200 nm, as indicated by the SEM images in Figure 5a,b. The EDX analysis

indicated the elemental compositions of the catalysts, with the signals pertaining to TiO_2 and ZnO, respectively, and a single carbon (C) peak appeared due to the use of carbon tape to fasten the samples during measurement.
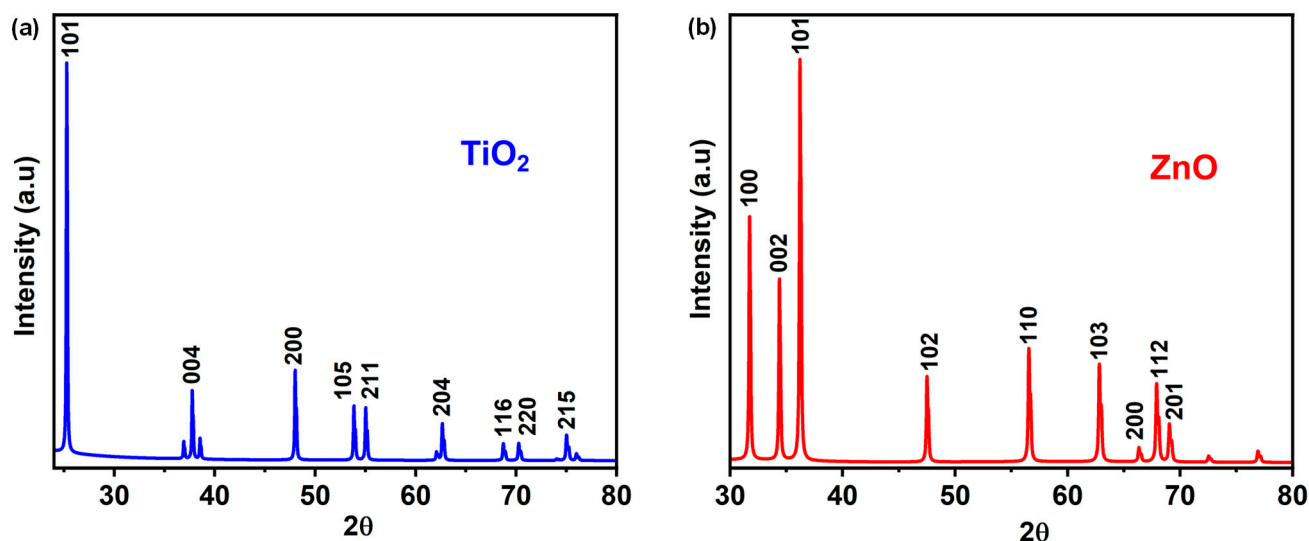
Figure 4. XRD patterns of (**a**) anatase titanium dioxide (TiO_2) and (**b**) zinc oxide (ZnO).
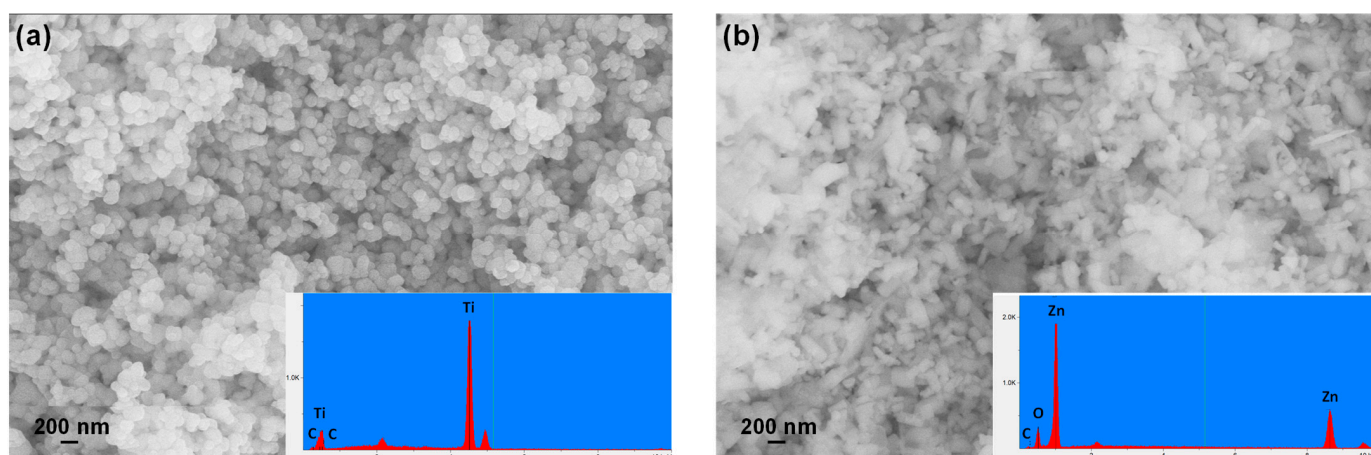
Figure 5. SEM images of (**a**) anatase titanium dioxide (TiO_2) and (**b**) zinc oxide (ZnO), with their EDX spectra included as insets.

It has been reported that the specific surface area (SSA) of a catalyst is another parameter that can affect the photocatalytic property of dyes' chemical decomposition [57,58]. The SSA of TiO_2 and ZnO was obtained via N_2 adsorption–desorption methods to ascertain the effect of SSA on the chemical decomposition of dyes. The SSA of ZnO (12.1 m^2/g) was higher than that of TiO_2 (5 m^2/g), and this physical parameter could relate to the higher catalytic activity over ZnO compared to TiO_2. The high SSA of ZnO means it adsorbs high amounts of CV chemicals, thus leading to an increase in the overall speed of CV degradation over time.

2.4. Reaction Kinetics

A kinetic study was performed to determine the applicable rate constant for the working catalysts. A common model used to represent the kinetics of organic dye degradation

is the Langmuir–Hinshelwood model [37]. The rate law equation and the corresponding integrated rate law are shown in Equations (1) and (2), respectively.

$$r = \frac{dC}{dt} = \frac{kKC}{1 + KC} \approx kKC \tag{1}$$

$$\ln\left(\frac{C_o}{C}\right) = kKt = k_{app}.t \tag{2}$$

where K is the adsorption equilibrium constant, k is the rate constant of the reaction, C is the CV concentration, and t is the reaction time. Since low concentrations of CV (highly diluted with water) were used in this study, it should be assumed that KC is much lower than 1 (KC << 1). The first-order rate law is shown in Equation (1). To confirm that the working catalysts follow the Langmuir–Hinshelwood model, concentration (C), ln (C), and 1/C as a function of reaction time, which correspond to zero-, first-, and second-order reactions, respectively, were investigated. As shown in Figure 6a,b, the ln (C) vs. time shows a linear line, indicating the first-order kinetics [59]. The rate constant (k_{app}), slope of the first-order plot of the ZnO (0.036 min^{-1}) was higher than that of TiO$_2$ (0.028 min^{-1}).
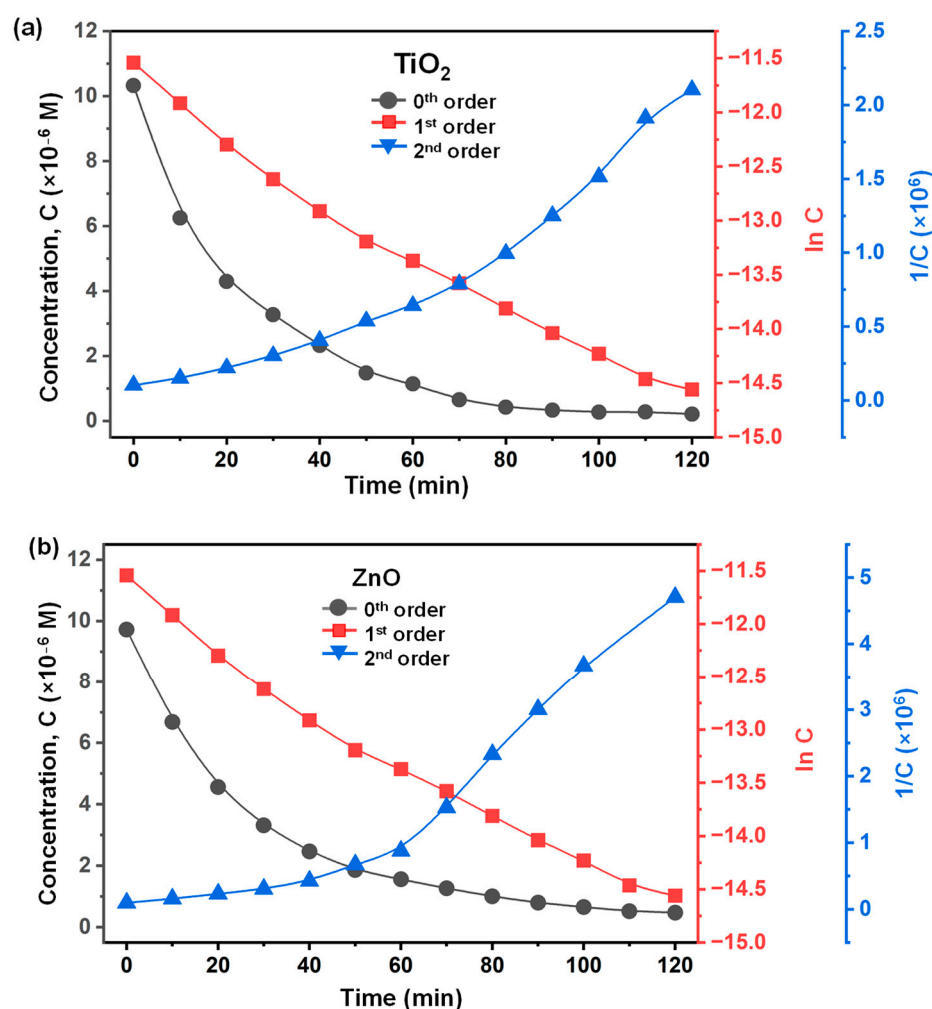
Figure 6. Kinetics of CV dye degradation. (**a**) Zero-, first-, and second-order kinetics plots for TiO$_2$-catalyzed CV degradation. (**b**) Zero-, first-, and second-order kinetics plots for ZnO-catalyzed CV degradation.

2.5. Proposed Mechanism

Although the reaction mechanism of CV degradation has not been thoroughly investigated, a series of photocatalytic and photosensitization processes can be used to describe its degradation [60]. The formed oxygen species from the water splitting reaction (OH•, $O_2^{•-}$ and HOO•) reacts with the electron–hole pairs on the photocatalyst, as well as the provided energy source, as can be seen in Equations (3)–(11) [29,37,38,60–62]. These reactions are necessary to produce reactive oxygen species (ROS), as well as a reaction with the chemisorbed CV dye for its degradation [60–62]. Photosensitized processes such as the reaction of the chemisorbed CV species with the provided energy on the surface of the photocatalyst can yield CV molecules in the excited state (CV*) [60]. The degradation of the dye can then proceed following the reaction of the CV* molecule with the electron–hole pairs and oxygen species [29,37,38,60–62]. Common radical scavengers such as ethylene diamine tetraacetic acid (EDTA-2Na; H^+ scavenger), isopropyl alcohol (IPA; OH• scavenger), and para benzoquinone (p-BQ; $O_2^{•-}$ scavenger) have been used in prior studies for the confirmation of the reaction mechanism [29]. The purpose of the scavengers is to "capture" the free intermediate radicals (H^+, OH• and $O_2^{•-}$) and indicate the role of the respective radicals depending on the change in activity due to their absence. Although the authors were unable to fully screen the mechanism of the reaction, we sought prior experimental instances from the literature in which radical scavengers were used to confirm our proposed mechanism of CV dye degrada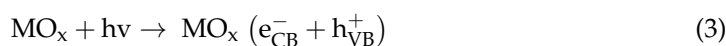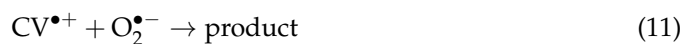tion by TiO_2 and ZnO. The formation of a hydroperoxyl radical (HOO•) from $O_2^{•-}$ is not a favored intermediate formation pathway, as proven by radical scavenger tests conducted in prior studies, since scavengers that capture H^+ and OH• radicals seem to have the highest loss in degradation capability when using a MO_x catalyst [29,61,62]. Although the generated $O_2^{•-}$ radicals may have some effect on activity, they are considered to be less reactive than H^+ and OH•, and therefore, they have been seen to reduce the rate of photocatalytic degradation only slightly [29,61,62]. The combination of these processes leads to the effective degradation of the dye pollutants, as shown by Equations (3)–(11) [33].

Photocatalytic Process:

$$MO_x + hv \rightarrow MO_x \left(e_{CB}^- + h_{VB}^+\right) \tag{3}$$

$$h_{VB}^+ + OH^- \rightarrow OH• \tag{4}$$

$$e_{CB}^- + O_2 \rightarrow O_2^{•-} \tag{5}$$

$$O_2^{•-} + H^+ \rightarrow HOO• \tag{6}$$

$$OH• + CV \rightarrow products \tag{7}$$

Photosensitization Process:

$$CV + hv \rightarrow CV^* \tag{8}$$

$$CV^* + MO_x \rightarrow CV^{•+} + MO_x \left(e_{CB}^-\right) \tag{9}$$

$$O_2^{•-} + e_{CB}^- + 2H^+ \rightarrow H_2O_2 \tag{10}$$

$$CV^{•+} + O_2^{•-} \rightarrow product \tag{11}$$
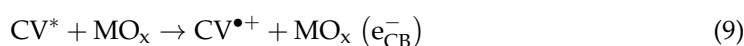
3. Experimental Section

3.1. Materials

A stock solution of 0.01 M CV (CAS# 548-62-9, ACS reagent, ≥90%, Sigma-Aldrich, St. Louis, MO, USA) solution and deionized water (~20 mΩ/cm, Direct-Q3, Millipore Sigma, Burlington, MA, USA) was used as a starting material to prepare CV solutions of different concentrations (1×10^{-6} M, 1×10^{-5} M, 2×10^{-5} M, 5×10^{-5} M, and 1×10^{-4} M). Titanium dioxide (TiO_2, nanoparticle, ≥99% purity, 4.26 g/mL at 25 °C), zinc oxide (ZnO, particle size: <5 μm, ≥99% purity), zirconium dioxide (ZrO_2, particle size: 5 μm, 99% purity, 5.89 g/mL at 25 °C), iron (III) oxide (Fe_2O_3, particle size: <5 μm, ≥96% purity),

copper (II) oxide (CuO, 99.99% purity), copper (I) oxide (Cu$_2$O, particle size: $\leq$7 µm, 97% purity, 6 g/mL at 25 °C), and niobium pentoxide (Nb$_2$O$_5$, 99.99% purity, 4.47 g/mL at 25 °C) were all obtained from Sigma-Aldrich and used without further treatment for the decomposition of CV solutions.

3.2. Characterization

The specific surface area (SSA) was obtained by a combination of N$_2$ adsorption and desorption isotherms using a Micromeritics ASAP 1010 instrument (Norcross, GA, USA). Prior to their analysis, each catalyst was degassed at 300 °C for 4 h under a vacuum for the removal of any possible impurities, moisture, and volatiles. The SSA was then calculated using a multipoint BET technique and recorded on the Quantachrome NovaWin©1994–2007 v10.0 software (Quantachrome Instruments, Boynton Beach, FL, USA). Raman spectra of the samples were obtained using a Horiba Xplora Plus Raman Microscope (Horiba Instruments Inc., Piscataway, NJ, USA) with a 532 nm laser source under ambient conditions. Raman spectra were collected in the 100 to 2000 cm^{-1} Raman shift regions. The operating parameters, with an acquisition time of 10 s and 10 scans, were kept constant throughout. XRD patterns were collected using a D8 Advance Bruker in reflection mode equipped with a Cu source (40 mV voltage and 40 mA current) and a 1D LYNXEYE detector. Powder was loaded into a side loading holder and leveled with a glass cover slip. XRD patterns were collected over a two-theta range of 10° to 100° with a step size set to 0.01°. During XRD pattern collection, specimens were rotated at a slow rpm to sample more powder and improve powder averaging. Match 3! v3.0 software, with the crystallography open database (COD), was utilized to identify all the phases. Energy-dispersive X-ray spectroscopy (EDX) was performed on a Leo 1550 scanning electron microscope (SEM) (ZEISS, New York, NY, USA), with data collected at a voltage of 20 kV loaded on a carbon tape sample holder. The UV-vis spectra were collected during CV degradation with a Tecan Infinite 200 PRO UV–visible spectrophotometer (TECAN, Morrisville, NC, USA) in the range of 230–1000 nm. The catalyst–dye solutions were evaluated for their absorbance after being centrifuged to minimize the presence of solid particles. An absorbance spectrum of 5 flash samples with a 2 nm step size was determined.

3.3. Activity Tests

For the CV decomposition reaction, 25 mg of metal oxide and 50 mL of CV solution were added into a 100 mL beaker containing a magnetic stirring bar. The beaker was transported to a UV cabinet (Mini UV Viewing cabinet, UVP, Inc., Upland, CA, USA, 95-0072-01, UVP C-10). Before exposing the CV solution with metal oxide to UV light, pre-stirring was performed for 60 min in a darkroom environment (i.e., a light-isolated environment with the UV light turned off) to ensure the homogenized mixing of catalysts and reactants. Following the pre-stirring step, the UV lamp (Handheld UV Lamp, UVP. LLC., 95-0005-05, UVGL-58) was turned on at the desired wavelength (i.e., 365 nm). During the reaction, 2 mL of the solution was collected at 10 min intervals and centrifuged at 3200 rpm for 5 min to separate the catalyst from the mixture. After centrifugation, 100 µL of the solution was extracted and put into three wells of a 96-well microplate (Corning™ Clear Polystyrene 96-Well Microplates, Corning, Glendale, AZ, USA) for analysis inside a Tecan UV Vis-spectrophotometer (Infinite Pro 200, TECAN, Morrisville, NC, USA). Absorbance data were collected 5 times from wavelengths of 230 nm to 1000 nm with a 2 nm step size. A schematic diagram of the reaction procedures and experimental conditions (i.e., time, speed) is shown in Scheme 1.
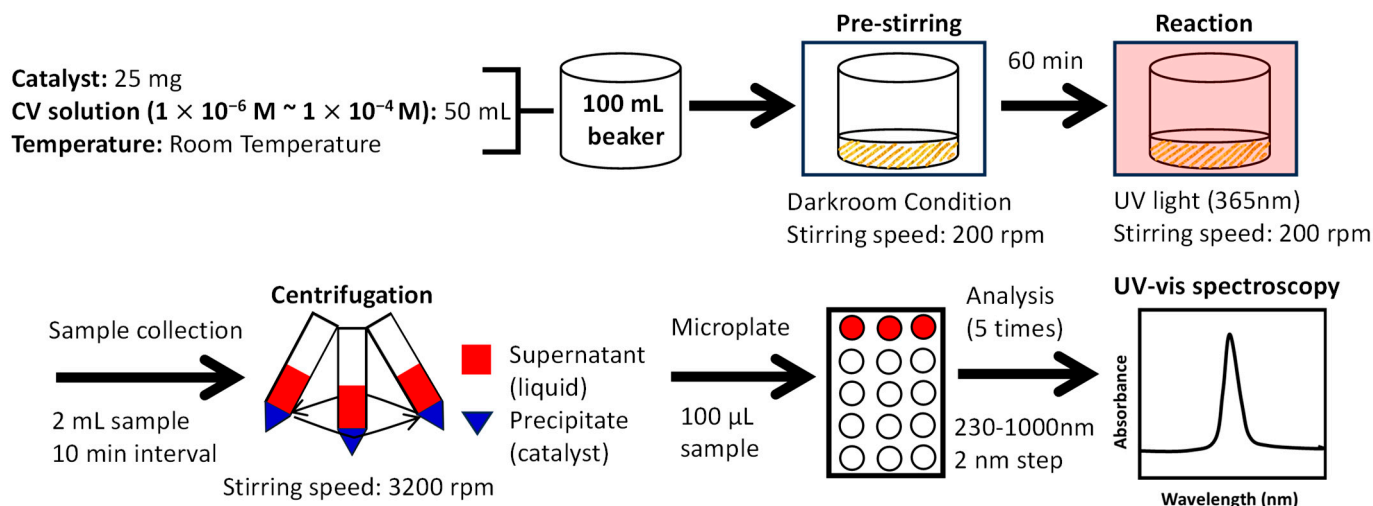
Scheme 1. Schematic of the reaction steps for the CV decomposition.

4. Conclusions

Different types of metal oxides, such as TiO_2, ZnO, ZrO_2, Fe_2O_3, CuO, Cu_2O, and Nb_2O_5, were evaluated for CV decomposition under UV irradiation conditions. Among the samples, TiO_2 and ZnO showed the highest catalytic performance, with 95% and 98% CV conversion values, respectively. Based on the quantitative analysis, it was observed that the reaction order is the first-order reaction, which follows the Langmuir–Hinshelwood model. The obtained rate constants over the ZnO and TiO_2 catalysts were 0.036 min^{-1} and 0.028 min^{-1}, respectively. The higher SSA of ZnO compared to TiO_2 could be related to the higher CV decomposition rate. The obtained results showed that photocatalytic parameters such as band gap, water splitting, specific surface area, and recombination rate control the dye chemical decomposition rate. For instance, the band gap energy of metal oxides is the driving factor in the dye chemical decomposition reaction. Furthermore, the band edges should match the water splitting potentials. To improve catalytic performance, supported metal oxide catalysts with high SSA values should be considered.

Author Contributions: M.S. was responsible for the development of the methodology, the investigation, writing (original draft and review and editing), and the visualization of the research. E.S. was responsible for the gathering of resources, the investigation, and writing (original draft and review and editing). A.S. and H.R. assisted in the investigation and writing (original draft and review and editing of final research). A.P. was responsible for the methodology and supervision. N.O. and D.J.S. were responsible for the XRD measurement. Y.M., H.-J.J. and G.H. were involved in the final writing stages (review and editing). Finally, T.K. was responsible for the conceptualization of the study, resources, supervision, project administration, and funding acquisition. All authors have read and agreed to the published version of the manuscript.

Data Availability Statement: The data that support the findings of the research are available on request from the corresponding author.

Conflicts of Interest: The authors declare no conflicts of interest.

References

1. National Library of Medicine. Compound Summary: Gentian Violet [Internet]. PubChem. 2024. Available online: https://pubchem.ncbi.nlm.nih.gov/compound/Gentian-violet (accessed on 26 August 2023).
2. Abbey Color. Crystal Violet. Abbey Color. Available online: https://abbeycolor.com/stains-and-reagents/crystal-violet/#:~:text=Crystal%20violet%20or%20methyl%20violet,as%20a%20moderate-strength%20external (accessed on 26 August 2023).
3. Mani, S.; Bharagava, R.N. Exposure to crystal violet, its toxic, genotoxic and carcinogenic effects on environment and its degradation and detoxification for environmental safety. *Rev. Environ. Contam. Toxicol.* **2016**, *237*, 71–104. [CrossRef]
4. DrugFuture. Gentian Violet [Internet]. DrugFuture–Chemical Index Database. Available online: https://www.drugfuture.com/chemdata/Gentian-Violet.html (accessed on 26 August 2023).
5. Khan, M.M.; Adil, S.F.; Al-Mayouf, A. Metal oxides as photocatalysts. *J. Saudi Chem. Soc.* **2015**, *19*, 462–464. [CrossRef]
6. Wu, J.; Gao, H.; Yao, S.; Chen, L.; Gao, Y.; Zhang, H. Degradation of crystal violet by catalytic ozonation using Fe/Activated Carbon Catalyst. *Sep. Purif. Technol.* **2015**, *147*, 179–185. [CrossRef]
7. Ledakowicz, S.; Paździor, K. Recent achievements in dyes removal focused on advanced oxidation processes integrated with biological methods. *Molecules* **2021**, *26*, 870. [CrossRef]
8. Qazi, U.Y.; Javaid, R.; Ikhlaq, A.; Al-Sodani, K.A.A.; Rizvi, O.S.; Alazmi, A.; Asiri, A.M.; Ibn Shamsah, S.M. Synergistically improved catalytic ozonation process using iron-loaded activated carbons for the removal of arsenic in drinking water. *Water* **2022**, *14*, 2406. [CrossRef]
9. Dellamatrice, P.M.; Silva-Stenico, M.E.; Moraes, L.A.; Fiore, M.F.; Monteiro, R.T. Degradation of textile dyes by cyanobacteria. *Braz. J. Microbiol.* **2017**, *48*, 25–31. [CrossRef]
10. Moradi, Z.; Jahromi, S.Z.; Ghaedi, M. Design of active photocatalysts and visible light photocatalysis. *Photocatal. Fundam. Process. Appl.* **2021**, *32*, 557–623. [CrossRef]
11. Ibhadon, A.; Fitzpatrick, P. Heterogeneous photocatalysis: Recent advances and applications. *Catalysts* **2013**, *3*, 189–218. [CrossRef]
12. Parrino, F.; Palmisano, G. Highlights on recent developments of heterogeneous and homogeneous photocatalysis. *Molecules* **2020**, *26*, 23. [CrossRef]
13. Bruggeman, D.F.; Mathew, S.; Detz, R.J.; Reek, J.N. Comparison of homogeneous and heterogeneous catalysts in dye-sensitized photoelectrochemical cells for alcohol oxidation coupled to dihydrogen formation. *Sustain. Energy Fuels* **2021**, *5*, 5707–5716. [CrossRef]
14. Alshamsi, F.A.; Albadwawi, A.S.; Alnuaimi, M.M.; Rauf, M.A.; Ashraf, S.S. Comparative efficiencies of the degradation of crystal violet using UV/hydrogen peroxide and Fenton's reagent. *Dyes Pigment.* **2007**, *74*, 283–287. [CrossRef]
15. Rehman, F.; Sayed, M.; Khan, J.A.; Sha, L.A.; Shah, N.S.; Khan, H.M.; Khattak, R. Degradation of crystal violet dye by Fenton and photo-fenton oxidation processes. *Z. Für Phys. Chem.* **2018**, *232*, 1771–1786. [CrossRef]
16. Fadhel, A.Z.; Pollet, P.; Liotta, C.L.; Eckert, C.A. Combining the benefits of homogeneous and heterogeneous catalysis with tunable solvents and Nearcritical Water. *Molecules* **2010**, *15*, 8400–8424. [CrossRef] [PubMed]
17. Chen, J.; Cen, J.; Xu, X.; Li, X. The application of heterogeneous visible light photocatalysts in organic synthesis. *Catal. Sci. Technol.* **2016**, *6*, 349–362. [CrossRef]
18. Ahmed, S.N.; Haider, W. Heterogeneous photocatalysis and its potential applications in water and wastewater treatment: A Review. *Nanotechnology* **2018**, *29*, 342001. [CrossRef]
19. Shelton's Water. Top 7 Methods of Water Treatment [Internet]. Kinetico Water Systems. 2015. Available online: https://sheltonswater.com/blog/top-7-methods-of-water-treatment (accessed on 26 August 2023).
20. Chen, C.; Chen, L.; Zhu, X.; Chen, B. Graphene nanofiltration membrane intercalated with AgNP@g-C$_3$N$_4$ for efficient water purification and photocatalytic self-cleaning performance. *Chem. Eng. J.* **2022**, *441*, 136089. [CrossRef]
21. Palani, G.; Apsari, R.; Hanafiah, M.M.; Venkateswarlu, K.; Lakkaboyana, S.K.; Kannan, K.; Shivanna, A.T.; Idris, A.M.; Yadav, C.H. Metal-doped graphitic carbon nitride nanomaterials for photocatalytic environmental applications-a review. *Nanomaterials* **2022**, *12*, 1754. [CrossRef]
22. Haider, A.J.; Jameel, Z.N.; Al-Hussaini, I.H.M. Review on: Titanium dioxide applications. *Energy Procedia* **2019**, *157*, 17–29. [CrossRef]
23. Sharma, D.K.; Shukla, S.; Sharma, K.K.; Kumar, V. A review on ZnO: Fundamental properties and applications. *Mater. Today Proc.* **2022**, *49*, 3028–3035. [CrossRef]
24. Tamirat, A.G.; Rick, J.; Dubale, A.A.; Su, W.-N.; Hwang, B.-J. Using hematite for photoelectrochemical water splitting: A review of current progress and challenges. *Nanoscale Horiz.* **2016**, *1*, 243–267. [CrossRef]
25. Sahoo, C.; Gupta, A.; Pal, A. Photocatalytic degradation of Crystal Violet (C.I. basic violet 3) on silver ion doped TiO$_2$. *Dyes Pigment.* **2005**, *66*, 189–196. [CrossRef]
26. Sanakousar, M.F.; Vidyasagar, C.C.; Jiménez-Pérez, V.M.; Jayanna, B.K.; Mounesh Shridhar, A.H.; Prakash, K. Efficient photocatalytic degradation of crystal violet dye and electrochemical performance of modified MWCNTs/Cd-ZnO nanoparticles with quantum chemical calculations. *J. Hazard. Mater. Adv.* **2021**, *2*, 100004. [CrossRef]
27. Shinde, D.R.; Tambade, P.S.; Chaskar, M.G.; Gadave, K.M. Photocatalytic degradation of dyes in water by analytical reagent grades ZnO, TiO$_2$ and SnO$_2$, A comparative study. *Drink. Water Eng. Sci.* **2017**, *10*, 109–117. [CrossRef]
28. Hussein, F.H.; Abass, T.A. Photocatalytic Treatment of Textile Industrial Wastewater. *Int. J. Chem. Sci.* **2010**, *8*, 1409–1420.

29. Puneetha, J.; Kottam, N.; Rathna, A. Investigation of photocatalytic degradation of crystal violet and its correlation with bandgap in ZnO and ZnO/GO nanohybrid. *Inorg. Chem. Commun.* **2021**, *125*, 108460.

30. Sharma, M.; Sondhi, H.; Krishna, R.; Srivastava, S.K.; Rajput, P.; Nigam, S.; Joshi, M. Assessment of GO/ZnO nanocomposite for solar-assisted photocatalytic degradation of industrial dye and textile effluent. *Environ. Sci. Pollut. Res.* **2020**, *27*, 32076–32087. [CrossRef]

31. Mageshwari, K.; Nataraj, D.; Pal, T.; Sathyamoorthy, R. Improved photocatalytic activity of ZnO coupled CuO nanocomposites synthesized by reflux condensation method. *J. Alloys Compd.* **2015**, *625*, 362–370. [CrossRef]

32. Suhail, F.S.A.; Mashkour, M.S.; Saeb, D. The Study on Photo Degradation of Crystal Violet by Polarographic Technique. *Int. J. Basic Appl. Sci.* **2015**, *15*, 12–21.

33. Wang, L.; Zhao, J.; Liu, H.; Huang, J. Design, modification and application of semiconductor photocatalysts. *J. Taiwan Inst. Chem. Eng.* **2018**, *93*, 590–602. [CrossRef]

34. Basith, M.A.; Ahsan, R.; Zarin, I.; Jalil, M.A. Enhanced photocatalytic dye degradation and hydrogen production ability of $Bi_{25}FeO_{40}$-rGO nanocomposite and mechanism insight. *Sci. Rep.* **2018**, *8*, 11090. [CrossRef]

35. Chowdhury, P.; Malekshoar, G.; Ray, A.K. Dye-Sensitized Photocatalytic Water Splitting and Sacrificial Hydrogen Generation: Current Status and Future Prospects. *Inorganics* **2017**, *5*, 34. [CrossRef]

36. Palani, R.; Anitha, V.; Karuppiah, C.; Rajalakshmi, S.; Li, Y.; Hung, T.; Yang, C. Imidazolatic-Framework Bimetal Electrocatalysts with a Mixed-Valence Surface Anchored on an rGO Matrix for Oxygen Reduction, Water Splitting, and Dye Degradation. *ACS Omega* **2021**, *6*, 16029–16042. [CrossRef]

37. Konstantinou, I.K.; Albanis, T.A. TiO_2-assisted photocatalytic degradation of azo dyes in aqueous solution: Kinetic and mechanistic investigations. *Appl. Catal. B Environ.* **2004**, *49*, 1–14. [CrossRef]

38. Ajmal, A.; Majeed, I.; Malik, R.N.; Idriss, H.; Nadeem, M.A. Principles and mechanisms of photocatalytic dye degradation on TiO_2 based photocatalysts: A comparative overview. *RSC Adv.* **2014**, *4*, 37003–37026. [CrossRef]

39. Axet, M.R.; Durand, J.; Gouygou, M.; Serp, P. Surface Coordination Chemistry on graphene and two-dimensional carbon materials for well-defined single atom supported catalysts. *Adv. Organomet. Chem.* **2019**, *71*, 53–174. [CrossRef]

40. Kim, T.; Burrows, A.; Kiely, C.J.; Wachs, I.E. Molecular/electronic structure-surface acidity relationships of model-supported tungsten oxide catalysts. *J. Catal.* **2007**, *246*, 370–381. [CrossRef]

41. Lee, K.M.; Brito, M.; DeCoster, J.; Linskens, K.; Mehdi, K.; Lee, W.I.; Kim, T. Influence of oxidizing and reducing pretreatment on the catalytic performance of CeO_2 for CO oxidation. *Mol. Catal.* **2022**, *528*, 112465. [CrossRef]

42. Zhang, S.; Li, Y.; Huang, J.; Lee, J.; Kim, D.H.; Frenkel, A.I.; Kim, T. Effects of Molecular and Electronic Structures in CoO_x/CeO_2 Catalysts on NO Reduction by CO. *J. Phys. Chem.* **2019**, *123*, 7166–7177. [CrossRef]

43. Zhang, S.; Kim, T. Effects of iron precursor and loading on the catalytic performance of FeO_x/CeO_2 catalysts for NO reduction by CO. *Mol. Catal.* **2020**, *494*, 111123. [CrossRef]

44. Ekoi, E.J.; Gowen, A.; Dorrepaal, R.; Dowling, D.P. Characterization of titanium oxide layers using Raman spectroscopy and optical profilometry: Influence of oxide properties. *Results Phys.* **2019**, *12*, 1574–1585. [CrossRef]

45. Jacob, K.A.; Peter, M.P.; Jose, P.E.; Balakrishnan, C.J.; Thomas, V.J. A simple method for the synthesis of anatase-rutile mixed phase TiO_2 using a convenient precursor and higher visible-light photocatalytic activity of Co-doped TiO_2. *Mater. Today Proc.* **2022**, *49*, 1408–1417. [CrossRef]

46. Ohtsuka, T.; Guo, J.; Sato, N. Raman spectra of the anodic oxide flim on titanium in acidic sulfate and neutral phosphate solutions. *J. Electrochem. Soc.* **1986**, *133*, 2473–2476. [CrossRef]

47. Arsov, L.D.; Kormann, C.; Plieth, W. Electrochemical synthesis and in situ Raman spectroscopy of thin films of titanium dioxide. *J. Raman Spectrosc.* **1991**, *22*, 573–575. [CrossRef]

48. Tang, H.L.; Ren, Y.; Wei, S.H.; Liu, G.; Xu, X.X. Preparation of 3D ordered mesoporous anatase TiO_2 and their photocatalytic activity. *Rare Met.* **2019**, *38*, 453–458. [CrossRef]

49. Ghosh, S.; Ghosh, A.; Pramanik, S.; Kuiri, P.K.; Sen, R.; Neogi, S.K. Synthesis of ZnO nanoparticles by co-precipitation technique and characterize the structural and optical properties of these nanoparticles. *J. Phys. Conf. Ser.* **2022**, *2349*, 012014. [CrossRef]

50. Song, Y.; Zhang, S.; Zhang, C.; Yang, Y.; Lv, K. Raman Spectra and Microstructure of Zinc Oxide irradiated with Swift Heavy Ion. *Crystals* **2019**, *9*, 395. [CrossRef]

51. Du, Y.; Zhang, M.S.; Hong, J.; Shen, Y.; Chen, Q.; Yin, Z. Structural and optical properties of nanophase zinc oxide. *Appl. Phys. A* **2003**, *76*, 171–176. [CrossRef]

52. Damen, T.C.; Porto, S.P.S.; Tell, B. Raman effect in Zinc Oxide. *Phys. Rev.* **1966**, *142*, 570. [CrossRef]

53. El-Deen, S.S.; Hashem, A.M.; Abdel Ghany, A.E.; Indris, S.; Ehrenberg, H.; Mauger, A.; Julien, C.M. Anatase TiO_2 nanoparticles for lithium-ion batteries. *Ionics* **2018**, *24*, 2925–2934. [CrossRef]

54. Silambarasan, M.; Saravanan, S.; Soga, T. Raman and photoluminescence studies of Ag and Fe-doped ZnO nanoparticles. *Int. J. ChemTech Res.* **2015**, *7*, 1644–1650.

55. Nagaraj, G.; Brundha, D.; Chandraleka, C.; Arulpriya, M.; Kowsalya, V.; Sangavi, S.; Jayalakshmi, R.; Tamilarasu, S.; Murugan, R. Facile synthesis of improved anatase TiO_2 nanoparticles for enhanced solar-light driven photocatalyst. *SN Appl. Sci.* **2020**, *2*, 734. [CrossRef]

56. Zaheer, A.; Ullahkha, F.; Mahmood, S.; Mahmood, T.; Shamim, A. Different Approaches for the Synthesis of Zinc Oxide Nanoparticles. *Open J. Chem.* **2018**, *1*, 19–25. [CrossRef]

57. Djurišić, A.B.; Leung, Y.H.; Ng, A.M.C. Strategies for improving the efficiency of semiconductor metal oxide photocatalysis. *Mater. Horiz.* **2014**, *1*, 400–410. [CrossRef]

58. Gahlot, S.; Dappozze, F.; Mishra, S.; Guillard, C. High surface area g-C$_3$N$_4$ and g-C$_3$N$_4$-TiO$_2$ photocatalytic activity under UV and Visible light: Impact of individual component. *J. Environ. Chem. Eng.* **2021**, *9*, 105587. [CrossRef]

59. Li, Y.; Xie, W.; Hu, X.; Shen, G.; Zhou, X.; Xiang, Y.; Zhao, X.; Fang, P. Comparison of dye photodegradation and its coupling with light-to-electricity conversion over TiO$_2$ and ZnO. *Langmuir* **2009**, *26*, 591–597. [PubMed]

60. Ju, Y.; Fang, J.; Liu, X.; Xu, Z.; Ren, X.; Sun, C.; Yang, S.; Ren, Q.; Ding, Y.; Yu, K.; et al. Photodegradation of crystal violet in TiO$_2$ suspensions using UV–vis irradiation from two microwave-powered electrodeless discharge lamps (EDL-2): Products, mechanism and feasibility. *J. Hazard. Mater.* **2011**, *185*, 1489–1498. [CrossRef] [PubMed]

61. Scott, T.; Zhao, H.; Deng, W.; Feng, X.; Li, Y. Photocatalytic degradation of phenol in water under simulated sunlight by an ultrathin MgO coated Ag/TiO$_2$ nanocomposite. *Chemosphere* **2019**, *216*, 1–8. [CrossRef]

62. Huang, S.; Chen, C.; Tsai, H.; Shaya, J.; Lu, C. Photocatalytic degradation of thiobencarb by a visible light-driven MoS$_2$ photocatalyst. *Sep. Purif. Technol.* **2018**, *197*, 147–155. [CrossRef]